AGU PUBLICATIONS

JGR

Journal of Geophysical Research: Atmospheres

RESEARCH ARTICLE
10.1002/2015JD024401

Key Points:
- Westward traveling planetary waves important to the elevated stratopause (ES) evolution and the stratopause recovery
- The impact of ES events extends well across the equator, altering the tropical wind, temperature, and ozone
- After ES events, the migrating semidiurnal tides amplify due to tropical stratospheric ozone and wind anomalies

Correspondence to:
V. Limpasuvan,
var@coastal.edu

Citation:
Limpasuvan, V., Y. J. Orsolini, A. Chandran, R. R. Garcia, and A. K. Smith (2016), On the composite response of the MLT to major sudden stratospheric warming events with elevated stratopause, *J. Geophys. Res. Atmos.*, *121*, doi:10.1002/2015JD024401.

Received 25 OCT 2015
Accepted 24 MAR 2016
Accepted article online 30 MAR 2016

On the composite response of the MLT to major sudden stratospheric warming events with elevated stratopause

Varavut Limpasuvan[1], Yvan J. Orsolini[2,3], Amal Chandran[4], Rolando R. Garcia[5], and Anne K. Smith[5]

[1]School of Coastal and Marine Systems Science, Coastal Carolina University, Conway, South Carolina, USA, [2]Norwegian Institute for Air Research (NILU), Kjeller, Norway, [3]Birkeland Centre for Space Science, University of Bergen, Bergen, Norway, [4]Laboratory for Atmospheric and Space Physics, Boulder, Colorado, USA, [5]National Center for Atmospheric Research, Boulder, Colorado, USA

Abstract Based on a climate-chemistry model (constrained by reanalyses below ~50 km), the zonal-mean composite response of the mesosphere and lower thermosphere (MLT) to major sudden stratospheric warming events with elevated stratopauses demonstrates the role of planetary waves (PWs) in driving the mean circulation in the presence of gravity waves (GWs), helping the polar vortex recover and communicating the sudden stratospheric warming (SSW) impact across the equator. With the SSW onset, strong westward PW drag appears above 80 km primarily from the dissipation of wave number 1 perturbations with westward period of 5–12 days, generated from below by the unstable westward polar stratospheric jet that develops as a result of the SSW. The filtering effect of this jet also allows eastward propagating GWs to saturate in the winter MLT, providing eastward drag that promotes winter polar mesospheric cooling. The dominant PW forcing translates to a net westward drag above the eastward mesospheric jet, which initiates downwelling over the winter pole. As the eastward polar stratospheric jet returns, this westward PW drag persists above 80 km and acts synergistically with the return of westward GW drag to drive a stronger polar downwelling that warms the pole adiabatically and helps reform the stratopause at an elevated altitude. With the polar wind reversal during the SSW onset, the westward drag by the quasi-stationary PW in the winter stratosphere drives an anomalous equatorial upwelling and cooling that enhance tropical stratospheric ozone. Along with equatorial wind anomalies, this ozone enhancement subsequently amplifies the migrating semidiurnal tide amplitude in the winter midlatitudes.

1. Introduction

The influence of a major sudden stratospheric warming (SSW) event (despite its name) extends beyond the stratospheric layer. In the past decade or so, troposphere-stratosphere coupling during SSWs has been a topic of much interest [e.g., *Kushner*, 2011]. Generated in the troposphere by sources like large-scale topography and land-sea thermal contrast, large-amplitude planetary waves (PWs) can propagate poleward as they penetrate upward into the stratosphere. Resulting PW Eliasen-Palm (EP) flux divergence in the upper stratosphere can decelerate the polar flow and induce a strong descent that promotes the observed polar stratospheric warming [*Matsuno*, 1971]. Subsequent interactions between PW and the circumpolar flow at lower altitudes help propagate the resulting wind and warm anomalies toward the tropopause, as noted by *Baldwin and Dunkerton* [2001]. The arrival of these anomalies there can induce momentum forcing by synoptic-scale waves that drives an overturning circulation to extend the anomalous westward wind to the surface [*Limpasuvan and Hartmann*, 2000; *Limpasuvan et al.*, 2004].

The impact of major SSWs can likewise extend upward into the mesosphere and lower thermosphere (MLT) [e.g., *Liu and Roble*, 2002; *Sassi and Liu*, 2014; *Wang et al.*, 2014]. At SSW onset, the aforementioned EP flux divergence in the upper stratosphere can elicit a polar mesospheric cooling above the stratospheric warming region [*Matsuno*, 1971; *Siskind et al.*, 2005]. During SSW, the ensuing wind reversal in the stratosphere further cools the mesosphere through the involvement of gravity waves (GWs). In propagating upward into the upper mesosphere, the dissipation of westward propagating and stationary GW typically drives an overturning circulation with downwelling over the winter pole that helps maintain the warm winter stratopause [*Hitchman et al.*, 1989]. However, the anomalous westward stratospheric wind during SSW limits the upward transmission of westward GW from the troposphere while allowing more upward propagation of eastward

GW [*Holton*, 1983; *Siskind et al*., 2010]. The westward GW drag in the upper mesosphere then diminishes, as eastward GW drag becomes more prominent. As a result, the GW-induced downwelling weakens, leading to a cooler mesosphere [*Garcia and Boville*, 1994] and the disappearance of the stratopause near its climatological position (~55 km).

As the vortex recovers from some major SSW events, observations in the upper mesosphere reveal that a new stratopause is formed around 80 km that eventually descends toward its typical position [*Manney et al*., 2008, 2009; *Orsolini et al*., 2010]. This "elevated stratopause" phenomenon [*Siskind et al*., 2010] is accompanied by an intense downwelling over the winter pole between 45 and 95 km [*Lee et al*., 2010]. The downwelling fosters intrusion of MLT air into the stratosphere and impacts polar chemistry [*Siskind et al*., 2007; *Manney et al*., 2008; *Kvissel et al*., 2012]. In particular, *Randall et al*. [2009] note an increased NO_x concentration ($NO + NO_2$) of mesospheric origin in the perturbed stratosphere after the 2008/2009 SSW, as the elevated stratopause falls. In the stratosphere, NO_x can be long-lived (a lifetime of months or longer) and can catalyze the destruction of ozone [*Randall et al*., 2005]. The changing stratopause characteristics during a major SSW and the associated upwelling can likewise impact the distribution of nighttime ozone in the 80–100 km layer [*Tweedy et al*., 2013].

In the lower thermosphere, recent studies suggest that major SSWs may elicit planetary-scale wave responses. *Limpasuvan et al*. [2012] and *Chandran et al*. [2013b] note the presence of westward, wave number 1 PWs in the winter high latitudes above 80 km after the onset of major SSW events with an elevated stratopause. *Chandran et al*. [2013b] find these PWs to have periods less than 10 days and suggest that the source of excitation is jet instability in the underlying polar mesosphere [*Sassi and Liu*, 2014]. Based on a SSW event in a high-top numerical model, *Liu and Roble* [2002] discuss the presence of in situ forced, quasi-stationary PWs in the upper mesosphere around the SSW onset. Potentially generated by momentum forcing associated with breaking GWs that had been filtered by planetary-scale, stratospheric wind variation [*Smith*, 1996, 2003], these quasi-stationary PWs can interact with tides to generate diurnal and semidiurnal wind variability in the MLT. *Goncharenko et al*. [2012] observe that an anomalous mean meridional circulation (induced by PW forcing in the stratosphere) can increase tropical stratospheric ozone mixing ratios by cooling the equatorial region, which in turn may enhance the forcing of migrating and nonmigrating semidiurnal tides as also observed by *Sridharan et al*. [2012]. On the other hand, *Sassi et al*. [2013] reported that changes in the meridional shear of the tropical upper stratospheric winds can enhance the tidal response following the 2009 SSW event by broadening the tropical waveguide, a mechanism initially proposed by *McLandress* [2002]. Potentially, the semidiurnal tide variability following the 2009 SSW event could be attributed to both the changing tropical wind and stratospheric ozone enhancement, as suggested by *Jin et al*. [2012].

At present, most of what we know about the MLT response to major SSWs has been based on case studies like those alluded to above. To develop a robust picture of the MLT response to major SSWs, we present in this paper the averaged characteristics of the MLT during the composite SSW life cycle. In particular, we focus on major SSW events that are accompanied by the elevated stratopause phenomenon (hereafter, referred to as ES-SSW). While not all major SSWs are accompanied by an elevated stratopause, *Chandran et al*. [2013a] demonstrates that ES-SSW events occur under conditions where the stratospheric jet, the GW forcing, and the mean meridional circulation remain reversed longer than in those winters when an SSW occurs without an ES. With such persistent anomalies, the selection of ES-SSW events should allow for a meaningful composite analysis. Furthermore, the presence of ES in these cases provides a clear visual evidence of the coupling between the stratosphere and the MLT.

Based upon a global climate-chemistry model that extends to about 145 km, the present study leverages global reanalyses to constrain the model evolution in the stratosphere and troposphere. As such, the ES-SSW events tend to parallel observations below ~50 km and reflect the modeled MLT response to SSW. With the zonal-mean composites of ES-SSW, we focus on the relative impacts of GWs and PWs in coupling the MLT to the stratosphere, through their momentum forcing, driving of the mean meridional circulation, and their roles in the ES formation. We also examine the extension of the circulation response to ES-SSW into the summer hemisphere and its potential connection to the amplification of tidal response in the lower thermosphere. The composite results exhibit the remarkable roles of wintertime PWs in driving the anomalous mean circulation in the presence of GWs, helping the polar vortex recover from the rapid warming and communicating the impact of the SSW to the summer hemisphere.

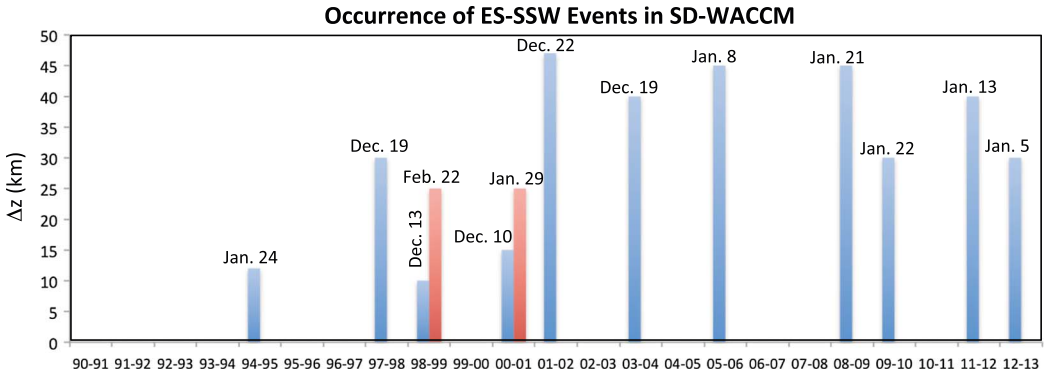

Figure 1. The 13 identified ES-SSW events in the SD-WACCM simulations used in the composite analysis. Each vertical bar indicates an event occurrence for a given Northern Hemisphere winter year (labeled on the horizontal axis). The height of the bar reflects the degree of stratopause vertical discontinuity (Δz) in kilometers. The red bar shows a second event in a given winter year. The onset date for each event is indicated above each bar.

2. Model and Methodology

In this study, we analyze output from the Whole Atmosphere Community Climate Model, Version 4 [*Marsh et al*., 2013] with specified dynamics (SD-WACCM) [*Marsh*, 2011] of the National Center for Atmospheric Research (NCAR). WACCM is a global circulation model with fully coupled chemistry and dynamics, has a horizontal resolution of 1.9° × 2.5° (latitude × longitude), and extends from the surface to ~145 km (with 88 pressure levels in all). The specified dynamics version relaxes the model's dynamics and temperature up to about ~0.79 hPa toward the Modern-Era Retrospective Analysis for Research and Application (MERRA) reanalyses of NASA's Global Modeling and Assimilation Office [*Rienecker et al*., 2011]. Above this nudged level, SD-WACCM transitions linearly to a free-running model and is fully interactive above 0.19 hPa. While nudging constrains the model's troposphere and stratosphere to follow the reanalyses, the meteorological and tracer response of SD-WACCM above 0.79 hPa has been shown to represent reasonably well the observed mesosphere and lower thermosphere [e.g., *Hoffmann et al*., 2012], particularly ES-SSW events [*Chandran et al*., 2013a, 2014; *Tweedy et al*., 2013; *De Wit et al*., 2014]. However, the polar downwelling strength associated with ES-SSW might be deficient in SD-WACCM [*Randall et al*., 2015; *Siskind et al*., 2015].

Runs of SD-WACCM are performed for each extended Northern Hemisphere winter (October through mid-April) from 1990 to 2013, using the initial condition on 1 October taken from existing daily SD-WACCM output. Model fields are output every 3 h. For each run, ES-SSW events are identified following the three criteria used by *Stray et al*. [2015]. Based on the polar cap averaged (70°N to 90°N) zonal-mean zonal wind and zonal-mean temperature between October and May of each winter, we require that (1) the temperature between 80–100 km falls below 190 K, (2) the reversal of the zonal-mean zonal wind from eastward to westward direction at the 1 hPa level (~50 km) persists for longer than 5 days, and (3) the stratopause altitude, based on the zonal-mean temperature maximum between 20 km and 100 km, as discussed by *Tweedy et al*. [2013], exhibits a discontinuity of at least 10 km in the vertical direction. This discontinuity marks the range of separation between the altitude to which the stratopause had descended following the onset of a SSW and the altitude at which a new stratopause reforms in the MLT during the recovery phase following the SSW. These selection criteria found 13 ES-SSW events, whose occurrences are shown in Figure 1. The length of each bar indicates the degree of stratopause separation (based on the polar cap average of the zonal-mean temperature) of the corresponding event. The onset dates of these events occur mainly in December (five events) and January (seven events). We note that the criteria used here differ from those of the World Meteorological Organization (WMO), and the identified events may occur during winters not identifiable as having major SSW events according to WMO. As noted by *Chandran et al*. [2013a], ES-SSW events are essentially polar cap phenomena and may not be associated with the zonal-mean zonal wind reversal at 10 hPa and 60°N, used in the WMO definition. Currently, no one uniform definition of ES-SSW exists, which, interestingly, may also be the case for SSW [*Butler et al*., 2015].

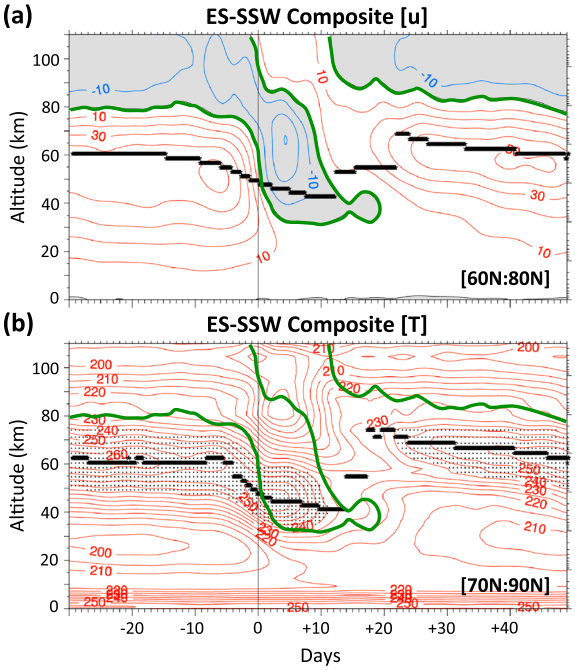

Figure 2. Altitude-time section of ES-SSW composite zonal-mean (a) zonal wind and (b) temperature. On the abscissa, time is relative to the ES-SSW onset (Day 0). Indicating eastward zonal wind direction, the red contours are plotted every 10 m s^{-1}. Indicating westward zonal wind direction, the blue contours are plotted every 10 m s^{-1}. The zero wind contour is in green. For temperature, the contour interval is every 5 K, with regions warmer than 240 K stippled to highlight the warm layer around the stratopause. For reference, the zero wind (green) contour from Figure 2a is repeated in Figure 2b. The latitudinal averaging band for these zonal-mean quantities is indicated in the lower right corner of each panel (e.g., from 60°N to 80°N for zonal wind). For each respective latitudinal average band, the approximate location of the stratopause is shown by the thick black line.

To develop a statistically robust picture of the ES-SSW characteristics, we perform a composite analysis. Each ES-SSW event is aligned in time such that Day 0 corresponds to the onset of the SSW, identified as the date when the zonal-mean zonal wind at 50 km switches from eastward to westward. We note that our selection of the onset day differs from the work of *Chandran et al.* [2013a]. These authors define Day 0 as the date when the reformed stratopause is at the highest altitude. This means that the onset date (Day 0) in our composites occurs some 10–15 days before the onset date of *Chandran et al.* [2013a].

3. Evolution of the Winter Polar Region

Figure 2 illustrates the altitude-time evolution of the composite zonal-mean zonal wind [*u*] and temperature [*T*]. Below approximately 80 km, the eastward wind rapidly weakens around Day −10 then switches to westward after Day 0. The eastward wind returns after approximately Day 15 and strengthens to a maximum speed around Day 35. Above 80 km, there is a wind reversal of opposite phase to that at lower altitudes, going from westward before SSW onset to eastward after onset and returning to the westward direction again around Day 15.

The temperature field undergoes alterations in conjunction with the wind field reversal. The SSW onset is characterized by the rapid descent of the stratopause (and the surrounding warm layer, stippled in Figure 2b) into the stratosphere, associated with the rapid warming that is indicative of SSW. By Day 10, the stratopause reaches its lowest altitude, around 40 km, as the eastward wind returns. Above the descended stratopause (and surrounding warm layer), the atmosphere up to 100 km undergoes tremendous cooling (by ~30 K compared to climatology, as shown below) in parallel with the stratospheric warming. A new warm layer and the stratopause reform around Day 20 near 80 km as the eastward wind begins to intensify. The magnitude of the stratopause discontinuity is approximately 40 km in the composite structure.

To further illuminate the changes associated with ES-SSW, we examine composite anomalies, defined as departures from climatology. As shown by Figure 1, many winters in our simulations experience ES-SSW events. In computing the climatology, we exclude winters that fulfill any of the criteria used to select ES-SSW events (noted in section 2). This strict exclusion removes major SSWs with ES and those without ES, since some major SSWs may fulfill only criterion (2) discussed in section 2. Careful examination of the results shows that computing the climatology this way produces a clear picture of the resulting anomalies. Here daily anomalies are computed for each ES-SSW event prior to composite averaging. While changes are sometimes better seen in anomalies, the interpretation of anomalies needs a careful treatment. For positive definite variables (like temperature or tracer concentration), the understanding of positive and negative anomalies is straightforward. For other variables, the anomalies need to be considered in the context of the climatological behavior.

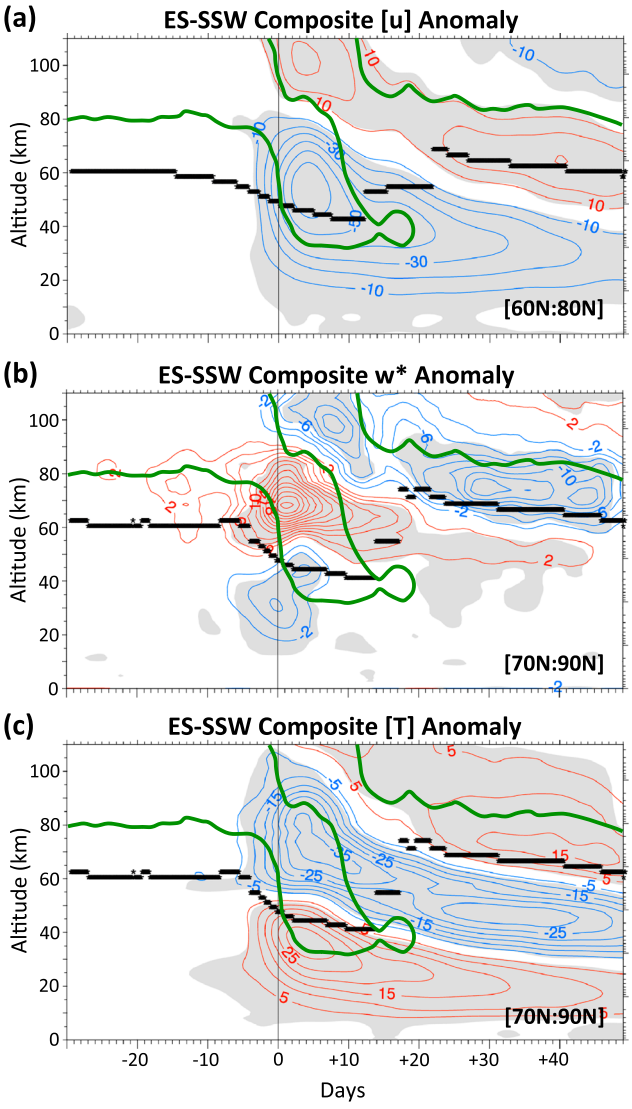

Figure 3. Altitude-time section of composite zonal-mean anomalies of (a) zonal wind (m s^{-1}), (b) TEM vertical velocity (mm s^{-1}), and (c) temperature (K). Red contours indicate positive anomalies. Blue contours indicate negative anomalies. Grey shadings show where the statistical significance level is above 95%. For reference, the zero wind from Figure 1 is overlaid on these panels along with the approximate location of the stratopause (thick black line).

Figure 3 shows the anomalies of [*u*], [*T*], and the transformed Eulerian mean (TEM) vertical velocity, *w**, based on the definition in *Andrews et al.* [1987]. The prevailing anomalous patterns tend to begin around the SSW onset and descend over time throughout the ES-SSW life cycle. In [*u*] and [*T*], significant anomalies extend nearly over the entire altitude range of the model. During the first 15 days after onset, strongest negative wind anomalies occur below 80 km and strongest positive anomalies occur above 80 km; these correspond to the wind reversals noted in Figure 2a. These changes occur in parallel with warming below 60 km and cooling aloft, with the temperature maxima appearing in near vertical quadrature with the wind anomalies during those 15 days after the onset (Figure 3c). After Day 15, the relatively smaller negative wind anomalies indicate the diminishing eastward stratospheric wind strength compared to climatology with warming below the descending core of the negative wind anomalies. During the recovery phase following the SSW, the positive wind anomalies appear with the reformed stratopause, along with warming of the entire MLT.

As shown by the grey shading, significant *w** anomalies occur above 10 km (Figure 3b). Around Day 0, negative *w** anomalies below 50 km denote enhanced downwelling in the polar region that accompanies the incipient stratospheric warming. Since climatological downwelling prevails in the 50 km to 80 km vertical range, the large positive *w** anomalies indicate weakened downwelling or even anomalous upwelling over the winter polar cap, as first discussed by *Siskind et al.* [2010]. Through the adiabatic effect, the weakened downwelling can lead to anomalous cooling. Thus, we see that the cooling anomalies in Figure 3c and the positive *w** anomalies descend in parallel (at least through Day 25). Strong negative *w** anomalies are also apparent above 80 km at SSW onset, which enhance the polar downwelling at those altitudes. This enhanced polar downwelling pattern continues to descend and, by Day 15, is associated with the anomalous warming and the newly reformed stratopause. We note that the tendency of temperature is negatively related to *w**. Thus, the rate of temperature decrease is strongest when upwelling is strongest, but the temperature minimum will occur after the time of maximum upwelling. This accounts for the displacement between the extrema of *w** and temperature anomalies seen in Figures 3b and 3c.

The impact of wave forcing during ES-SSW is shown in Figure 4. Over much of the winter hemisphere, the resolved waves, as diagnosed with the EP flux divergence, provide a robust westward drag during ES-SSW.

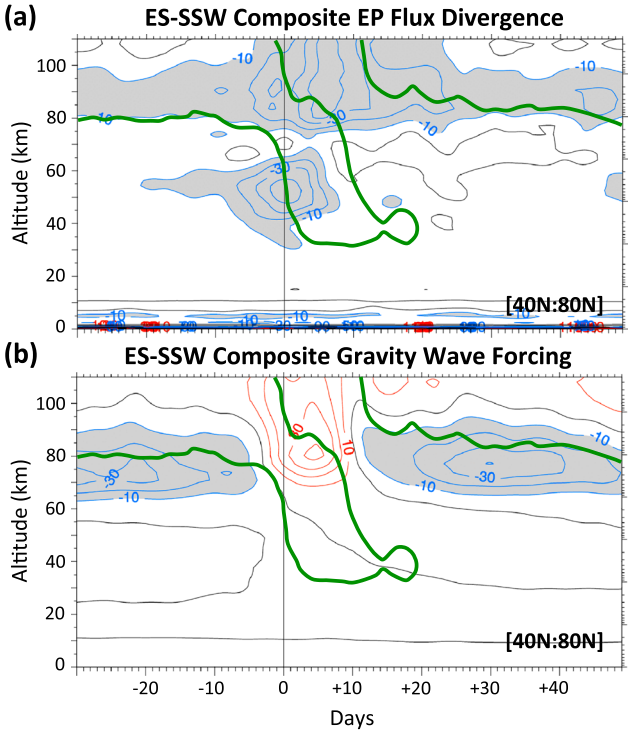

Figure 4. As in Figure 2, but for (a) the resolved EP flux divergence and (b) zonal-mean gravity wave forcing. Red contours indicate positive (eastward) acceleration every 10 m s^{-1} d^{-1}. Blue contours indicate negative (westward) acceleration every 10 m s^{-1} d^{-1}. The zero acceleration contour is in black. Grey shadings are regions where the magnitude of negative acceleration is at least 10 m s^{-1} d^{-1}. For reference, the zero wind (green contour) from Figure 1 is overlaid on these panels.

In analyzing Figure 1, we noted 80 km as roughly the altitude separating the out-of-phase zonal wind reversals. This 80 km boundary also divides the resolved wave forcing. Below 80 km, the core westward drag (exceeding 40 m s^{-1} d^{-1}) peaks on Day 0 as [*u*] undergoes strong negative tendency in Figure 2. Above 80 km, the resolved westward drag maximizes around Day 5 and extends well above 100 km.

In the model, GW forcing is parameterized by considering wave sources due to orography, frontogenesis, and convection [*Richter et al.*, 2010]. Contributions from frontogenesis lead to the greatest GW drag in the winter polar region, while convection plays a negligible role (not shown). As shown in Figure 4b, the composite GW forcing tends to maximize near 80 km. Climatologically, the westward GW drag around this level is associated with maintaining the stratopause by driving a polar downwelling [*Hitchman et al.*, 1989].

As the underlying westward drag by the resolved waves intensifies with SSW onset, the eastward stratospheric wind slows down. The diminished eastward wind allows more eastward propagating GW to reach the MLT, which results in the weakening westward GW drag shown in Figure 4b around Day −10. As the underlying stratospheric wind begins to switch to the westward direction, the westward propagating GWs are absorbed in the stratosphere and more eastward propagating GWs are allowed to reach higher altitudes [e.g., *Holton*, 1983; *Liu and Roble*, 2002]. Ultimately, the dissipation of eastward propagating GWs imposes an eastward drag seen around Days −5 to 10. The growth of eastward GW drag, peaking around SSW onset, was observed between 90 and 100 km in the 2012–2013 ES-SSW using local meteor radar observations over Trondheim, Norway [*De Wit et al.*, 2014]. As the eastward wind below 60 km is reestablished, a similar filtering process leads to the reappearance of westward GW drag near 80 km and formation of the new stratopause.

4. Meridional Cross Sections of Key Stages

Based on the location of the zero wind line of the previous figures, we see that most of the drastic changes in the ES-SSW tend to occur over the first 20 days after the SSW onset. During this critical period, a remarkable evolution occurs in the resolved wave and parameterized GW forcings as the wind and temperature structures change and recover toward climatology. Here we further study this period by computing time averaged meridional cross sections over two stages: Stage I is the period from Day 0 to Day 10, and Stage II is the period from Day 10 to Day 20. The meridional extent of wave forcing, [*u*], and [*T*] during Stages I and II are illustrated in Figures 5 and 6, respectively.

In Stage I, the westward wind (dashed contours) is evident in the polar winter hemisphere between 40 km and 90 km and the eastward mesospheric jet is confined to the low winter latitudes. Diagnosed by regions of EP flux convergence, the westward drag due to the resolved waves is largest in the winter hemisphere near the zero wind line (Figure 5a). Consistent with Figure 4a, this westward drag is centered around 50 km and

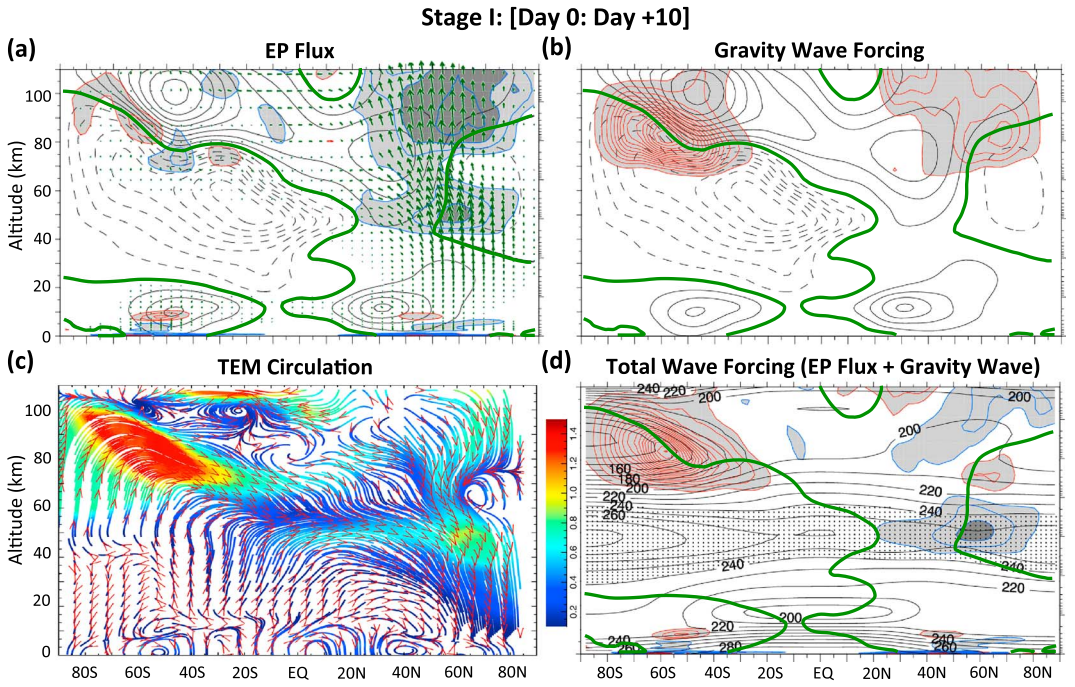

Figure 5. Meridional, time averaged cross sections of ES-SSW composites for (a) resolved wave forcing, (b) gravity wave forcing, (c) TEM circulation, and (d) total wave forcing for Day 0 to Day 10 (Stage I). All wave forcing is shown in blue (westward) and red (eastward) contours (every 10 m s^{-1} d^{-1}, excluding zero). Westward forcing in excess of 30 m s^{-1} d^{-1} are shaded in dark grey. In Figure 5a, the EP flux is shown as green vectors. The TEM circulation is shown as curly vectors. The red arrow heads (V) indicate the (v^*, w^*) vector direction while the background colors show the vector magnitude (divided by 10) computed after w^* is scaled by 1000. Here, v^* is the TEM meridional velocity. Where v^* is strongest, the color bar has a unit of dam s^{-1}. Where w^* is strongest, the color bar has a unit of cm s^{-1}). In Figures 5a and 5b, the zonal-mean zonal wind is shown in black contours (every 10 m s^{-1}). Solid contours indicate eastward winds and dashed contours westward winds. In Figure 5d, the zonal-mean temperature is shown in black contours (every 10 K) with middle atmospheric layer warmer than 240 K stippled (like in Figure 1). The zero wind contour is denoted by the bold green line and shown in Figures 5a, 5b, and 5d for reference.

above 80 km. In the meridional cross section, we see that the overall westward drag at the lower altitudes is smaller in magnitude and more limited in latitudinal extent than the overlying westward drag. Consistent with Figure 4b, the GW drag above 80 km in the winter hemisphere is eastward during this period due largely to the filtering effect of the underlying polar westward wind. While this eastward GW drag tends to counteract the westward drag of the resolved waves, the total wave forcing (represented by the sum of GW forcing and EP flux in Figure 5d) is still negative. This net westward drag in winter polar MLT reveals the dominance of momentum forcing by the resolved waves in that altitude range.

Around 50 km, the strongest net westward drag (nearly all attributable to the resolved waves) drives a strong TEM circulation (Figure 5c), characterized by upwelling in the tropics and downwelling near the polar winter latitudes, with strong northward motion throughout the winter midlatitudes near 50 km. The polar downwelling is manifested as a negative w^* anomaly in Figure 3b below 50 km. This downwelling appears in conjunction with the descending stratopause, seen in Figure 5d as a stippled warm layer (centered around 40 km) in the background temperature contour (see also, Figure 2b). In the Northern Hemisphere MLT, the enhanced polar downwelling occurs between 80 km and 100 km (as noted by the negative w^* anomaly between Day 0 and Day 10 of Figure 3b). This descent appears to be driven in part by the net westward drag (dominated by the resolved wave forcing) seen in Figure 5d above 80 km and poleward of 40°N.

Between 60 km and 80 km, Northern Hemispheric downwelling deviates toward the midlatitudes, as indicated by the presence of a counterclockwise gyre centered around 65°N (Figure 5c). This gyre interrupts the climatological polar downwelling (and associated warming) between 60 km and 80 km and is thus consistent with the positive w^* anomaly and cooling anomaly, evident in Figures 3b and 3c. As seen in Figure 5d, the net eastward drag in the total wave forcing (dominated by GW forcing) near 60°N and 70 km appears to drive this gyre.

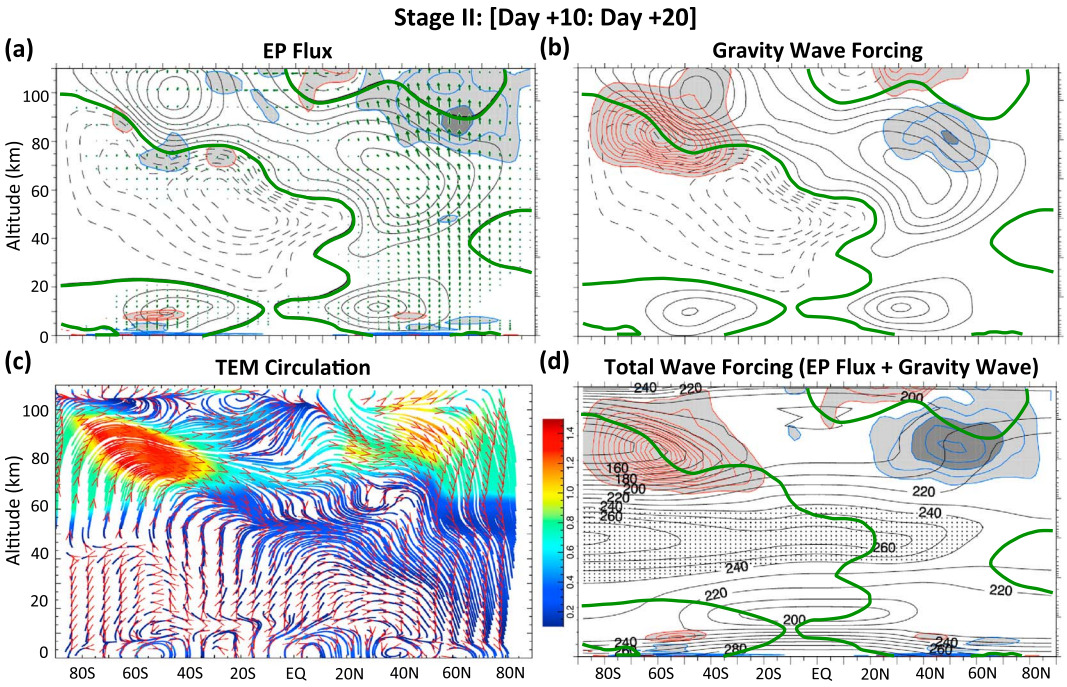

Figure 6. Same as Figure 5, except for the period from Day 10 to Day 20 (Stage II). The EP vector lengths in Figure 6a are scaled relative to the same reference vector length used in Figure 5a. As such, we can see the relative growth/decay in EP vector from Stage I (in Figure 5a) to Stage II.

Liu and Roble [2002] identify a very similar counterclockwise cell near the winter pole in their SSW simulation using the NCAR Thermosphere, Ionosphere, Mesosphere, and Electrodynamics General Circulation Model (TIME-GCM).

In Stage II (Figure 6), we see that the eastward mesospheric jet has strengthened and displaced the anomalous westward wind, characteristics associated with the SSW recovery. Between 80 km and 100 km, the total wave forcing imposes a strong net westward drag in the winter hemisphere (Figure 6d). Figures 6a and 6b show that this net westward drag is the combined result of the westward drag of resolved waves and GWs. As demonstrated by Figure 4a (by the persistent westward drag above 80 km), the impact of the resolved waves above the eastward mesospheric jet in Stage II appears to linger from Stage I.

The stratospheric mean meridional circulation seen in Stage I has greatly diminished in strength and latitudinal range in Stage II. Subsequently, the strong downwelling in the winter polar stratosphere disappears along with the stratopause (see Figure 3b), as noted by the absence of the warm stippled layer poleward of 60°N in Figure 6d. On the other hand, the northward motion and polar downwelling in the winter MLT have greatly intensified relative to Stage I. This enhanced downwelling over the winter polar region between 70 km and 100 km is reflected in the large negative w^* anomaly in Figure 3b at this altitude range.

In Figures 5 and 6, the meridional cross section extends into the summer hemisphere for completeness. In the Southern Hemisphere, the net eastward drag (mainly due to GW forcing) is the dominant feature above the summer mesospheric jet in Stages I and II. This eastward drag drives the persistent clockwise circulation centered near 70 km and 40°S, giving rise to an intense polar upwelling that adiabatically cools the summer mesopause, which is the very cold region ($T < 140$ K) seen in the background temperature field. Between 20°S and 60°S, near 70–80 km, we note a region of alternating westward and eastward drag by the resolved waves (Figures 5a and 6a). Closer examination shows that these features are associated with the quasi two day wave (QTDW) family, which often amplifies after the winter solstice in the summer hemisphere [*Wu et al*., 2008; *Limpasuvan et al*., 2005]. This wave family consists of zonal wave numbers 3 and 4, with westward propagating period between 1.5 and 2.2 days, along with some contributions from zonal wave number 1 of similar phase speed.

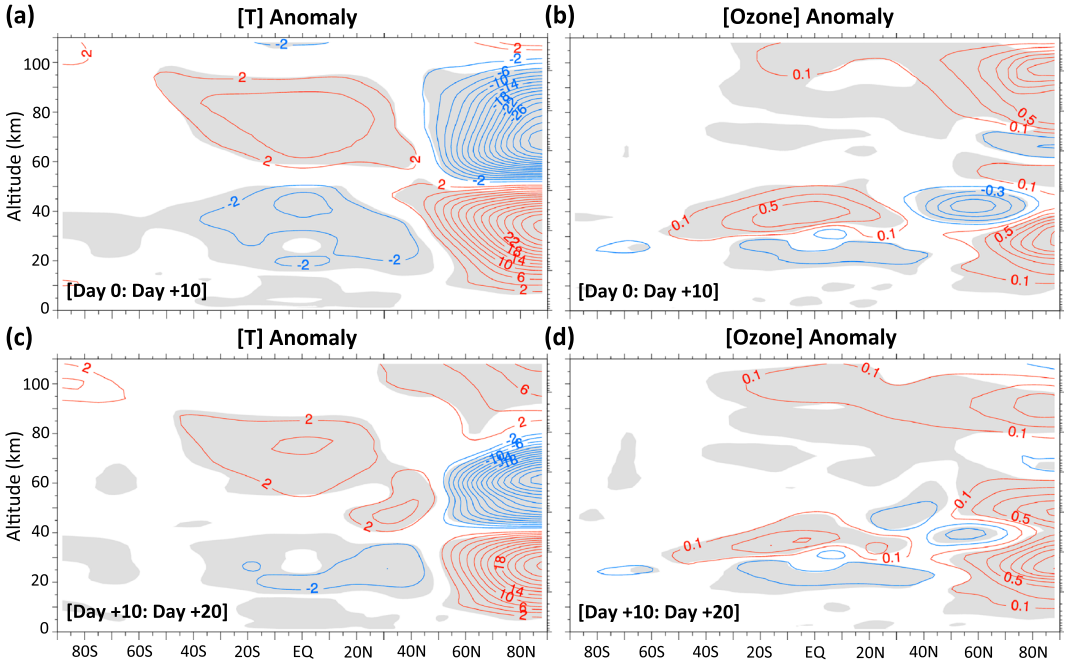

Figure 7. Meridional cross sections of ES-SSW composite zonal-mean (a, c) temperature anomaly and (b, d) ozone anomaly. Figures 7a and 7b show the time-averaged period from Day 0 to Day 10. Figures 7c and 7d show the time-averaged period from Day 10 to Day 20. Red contours indicate positive anomalies. Blue contours indicate negative anomalies. Grey shadings are regions where the statistical significance level exceeds 95%.

The impact of the mean meridional circulation (induced by GW and PW drag noted in Figures 5 and 6) on the temperature and ozone is shown in Figure 7. To highlight these impacts, we display anomalies of these positive definite variables with respect to climatology. In Stage I (Figures 7a and 7b), we see a pair of horizontally stacked dipole structures in the [*T*] anomaly. Below 50 km, the dipole structure consists of a negative anomaly centered over the equator and a positive anomaly over the winter pole, like the observations of *Randel* [1993]. This pattern is associated with the clockwise stratospheric circulation (Figure 5c), with tropical upwelling that results in negative [*T*] anomaly through adiabatic cooling and polar downwelling that results in positive [*T*] anomaly through adiabatic warming. This cooling of the tropical stratosphere during SSW events is also documented by *Fritz and Soules* [1970] and *Randel* [1993]. Above 50 km, the dipole structure is opposite in phase to the dipole below. In Stage I, the equatorial warm anomalies appear to be associated with the tropical downwelling between 50 km and 80 km that converges with the underlying tropical upwelling, merging to become part of the strong northward flow around 50 km. This equatorial warming above 50 km may be driven by the westward wave forcing in the winter upper stratosphere (cf. Figure 5c). As this northward flow diminishes in Stage II, the tropical downwelling and warming anomaly above 50 km also subside.

The corresponding changes in ozone are more complicated because of its varying photochemical lifetime and transport by the TEM circulation. Below 50 km, the quadruple-like structure of ozone anomaly consists of strong positive values near 40 km over the equatorial region and near 30 km poleward of 50°N (Figure 7b). This structure is reminiscent of the observed ozone distribution shown in Figure 5 of *Randel* [1993] for SSWs. The positive ozone anomaly in the equatorial region is most likely due to the overlapping cold anomaly in the tropical stratosphere, induced by equatorial upwelling. Such a cold anomaly will decrease ozone loss in the Chapman cycle by slowing the rate of the $O + O_3$ reaction, which is a sink of odd oxygen. Additionally, the lowered temperature can reduce the effectiveness of catalytic loss cycles involving HO_x, NO_x, and ClO_x. In this altitude range, the odd oxygen photochemical lifetime is on the order of a day or less, so transport does not play a direct role in ozone photochemistry. Indeed, *Goncharenko et al.* [2012] observe that the mean circulation (driven by resolved waves) may increase the tropical ozone concentration in the 30–50 km layer by cooling the equatorial region.

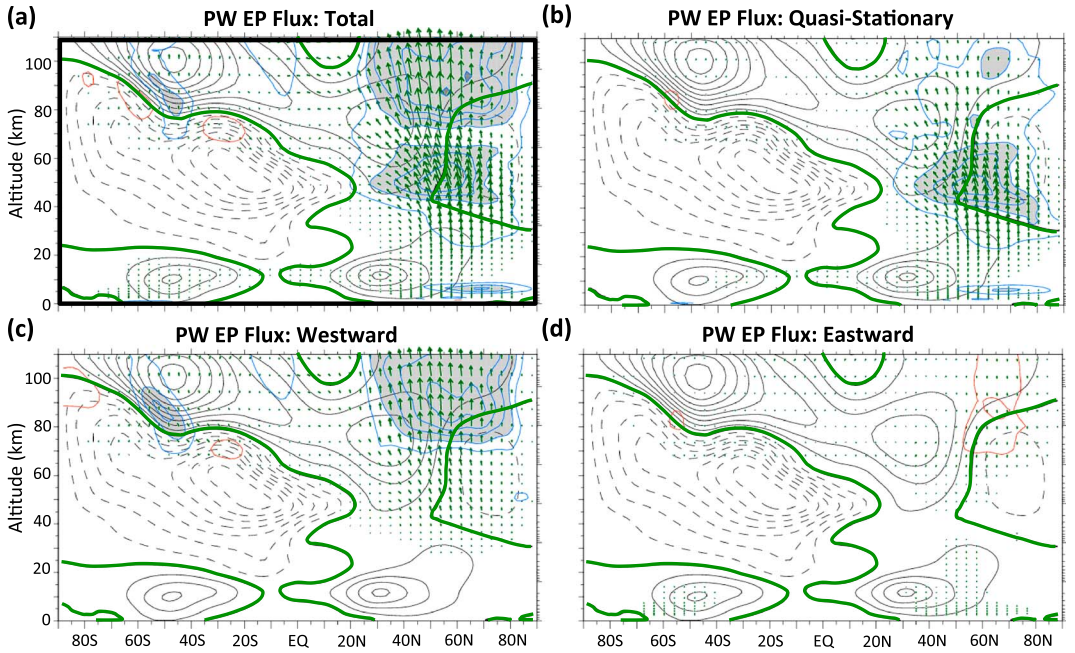

Figure 8. Meridional cross sections of ES-SSW composite EP flux (green vectors) and its divergence (red/blue contours, at 5 m s^{-1} d^{-1} intervals, shaded above absolute values of 10 m s^{-1} d^{-1}) for (a) all planetary waves (PWs), (b) quasi-stationary PWs, (c) westward propagating PWs, and (d) eastward propagating PWs. Red contours indicate positive (eastward) acceleration. Blue contours indicate negative (westward) acceleration. In all panels, the corresponding zonal-mean zonal wind is shown in black contours (every 10 m s^{-1}). Solid contours denote eastward winds and dashed contours westward winds. The zero wind contour is shown in bold green line. All values are averaged over the first 10 days after SSW onset (i.e., Day 0 through Day 10; Stage I). Here all PWs are associated with zonal wave numbers 1–4. All vectors are scaled to the same reference vector.

We also note the ozone enhancement in the polar MLT region where the secondary ozone layer is located [e.g., *Smith et al*., 2009]. Although ozone abundance in this layer is greatest at nighttime, and the ozone plots in Figure 7 do not exclude daytime values, the positive anomaly in the MLT ozone is consistent with the findings of *Tweedy et al*. [2013]. These authors found that polar cooling and diminished concentration of atomic hydrogen (a sink of ozone), attributable to the anomalous polar upwelling, lead to the enhancement of ozone concentration and the upward deflection of the secondary ozone layer.

In Stage II (Figures 7c and 7d), the features noted in Stage I generally persist, although with some downward displacement of anomalies in the winter polar region, as seen also in Figure 3. Consistent with the weakened and spatially diminished clockwise stratospheric mean meridional circulation cell, the decreased tropical upwelling results in less cooling of the tropics and smaller positive tropical ozone anomaly. The intensified clockwise circulation cell in the winter MLT (Figure 6c) and associated strong polar downwelling are linked to the significant warming anomaly above 90 km. This polar downwelling also brings down the ozone anomaly associated with the secondary ozone maxima as reported by *Tweedy et al*. [2013].

5. Resolved Waves and Their Impact

In Figure 8, we show the EP flux divergence due only to PWs of zonal wave numbers 1 through 4 during Stage I. Given the similarity of the wintertime westward drag between Figures 8a and 5a, we conclude that these PWs account for nearly all resolved waves in the middle atmosphere. In the remaining panels of Figure 8, we divide the PW forcing according to the phase propagation direction of the waves using band-pass filtering. Here westward and eastward waves consist of waves with westward and eastward propagating phases that have periods longer than 1 day but shorter than 20 days. This definition excludes eddy fluxes due to atmospheric tides. Quasi-stationary waves are defined as the combined westward and eastward signals whose periods are longer than 20 days.

From Figures 8b and 8c, we see that different types of PWs contribute to the westward drag in two distinct altitude ranges. Between 40 km and 70 km, the PW westward drag is almost exclusively due to quasi-stationary

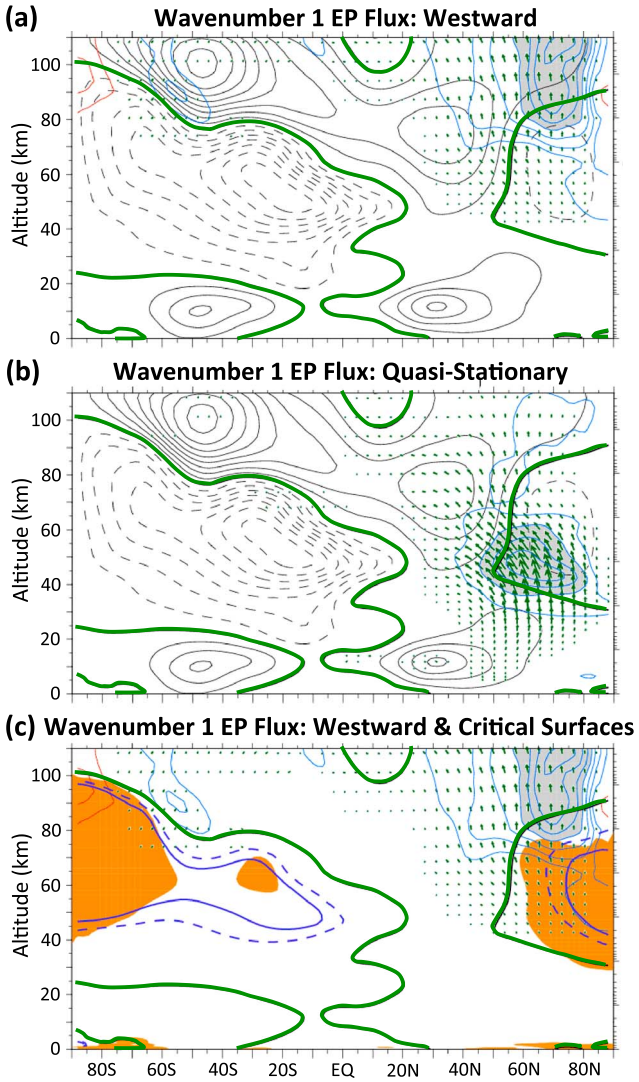

Figure 9. Meridional cross sections of ES-SSW composite wave number 1 planetary wave EP flux (green vectors) and its divergence (red/blue contours) for (a) westward propagating waves with divergence at 5 m s^{-1} d^{-1} intervals and (b) quasi-stationary waves with divergence at 10 m s^{-1} d^{-1} intervals (to avoid cluttering of contours). Shaded above absolute values of 20 m s^{-1} d^{-1}, red contours indicate positive (eastward) acceleration and blue contours negative (westward) acceleration. (c) Same as in Figure 9a except the orange regions show regions where the meridional gradient of the mean quasi-geostrophic potential vorticity is negative. Also in Figure 9c, the critical surfaces associated with wave number 1 of westward 7 day period and 10 day period are shown in solid and dashed purple lines, respectively. In Figures 9a and 9b, the corresponding zonal-mean zonal wind is shown in black contours (every 10 m s^{-1}). Solid contours denote eastward winds and dashed contours westward winds. The zero wind contour is shown in bold green line and repeated in Figure 9c. All values are averaged over the first 10 days after SSW onset (i.e., Day 0 through Day 10; Stage I).

waves. Above 70 km, PW forcing by westward propagating waves dominates the westward drag in the winter hemisphere (and summer hemisphere due to the QTDW family). This behavior was also reported by *Chandran et al.* [2013b]. Eastward drag by eastward propagating PWs is negligible compared to the other PW components (Figure 8d).

The PW westward drag in the 40–70 km layer and in the layer above 70 km is associated mostly with zonal wave number 1 as shown in Figures 9a and 9b. The evolution of the power spectrum of zonal wave number 1 in these two layers can be seen in Figure 10. Here a spectral analysis is performed on the zonal wave number 1 meridional wind (v) based on a 30 day sliding window for the time series of each ES-SSW event. Sliding the analysis window allows the evolution of the frequency/period with respect to time to be observed. Similar results are obtained using a Morlet wavelet analysis, as done by *Chandran et al.* [2013b]. Averaged between

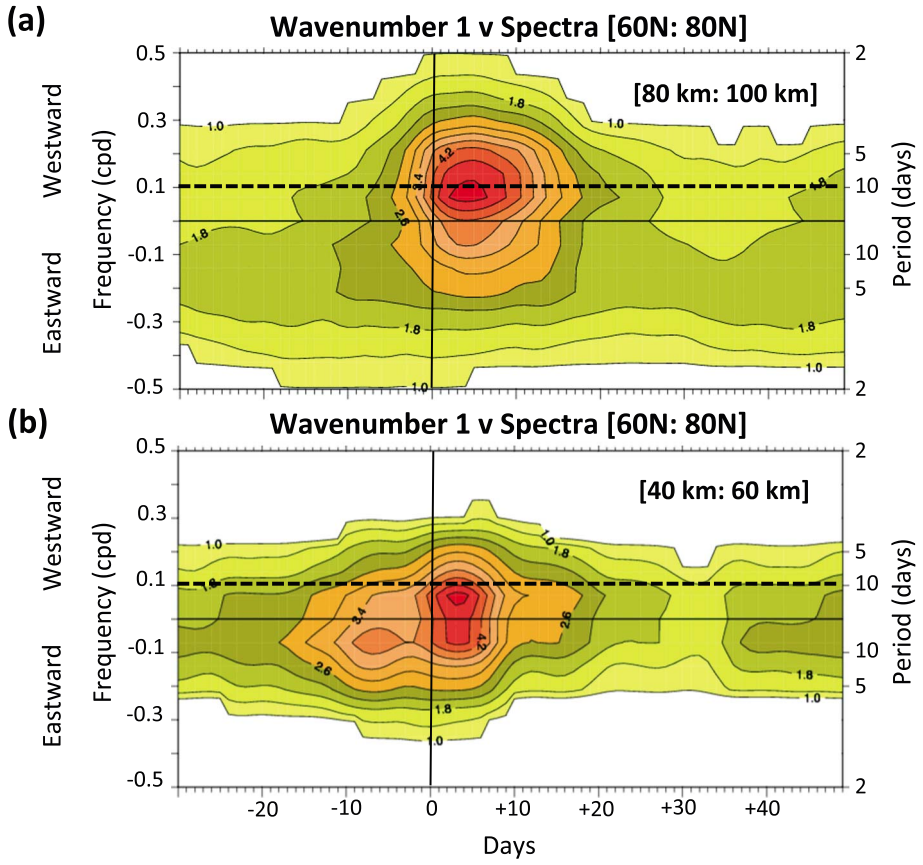

Figure 10. Frequency/period evolution over time of ES-SSW composite wave number 1 spectra of meridional wind averaged between 60 N and 80 N and between the (a) 80 km to 100 km layer and (b) 40 km to 60 km layer. On the horizontal axis, time is relative to the ES-SSW onset (i.e., Day 0). For reference, the horizontal dashed black line indicates a westward period of 10 days.

60°N to 80°N, the ES-SSW composite of the spectral evolution is shown in Figure 10a for the layer between 80 km and 100 km and in Figure 10b for the layer between 40 km and 80 km. These layers correspond to the altitude range where we noted strong westward drag in Figure 8.

In the 40–60 km layer, Figure 10b shows that the zonal wave number 1 spectral power increases broadly around the SSW onset day. The spectral peak is largely confined in the frequency band of −0.1 and +0.1 cycles per day and appears consistent with the quasi-stationary wave EP flux in Stage 1, shown in Figure 9b. At a higher level (Figure 10a), the zonal wave number 1 spectral power is shifted toward westward period with most of the signal between 5 and 12 days. While the 30 day sliding approach tends to smear the spectral signal in time, it is clear that much of the spectral peak at the higher altitude range appears mainly westward after Day 0.

The composite shown in Figure 9c suggests that the cause of the westward zonal wave number 1 activity may be jet instability in the winter polar region. Based on the spectral peak in Figure 10a, the critical surfaces of wave number 1 perturbation with westward periods of 7 and 10 days are plotted on the meridional cross sections of Figure 9c as solid and dashed purple lines. While these westward wave periods may be Doppler shifted to zero in the summer westward jet, these critical surfaces are anomalous occurrences in the polar winter hemisphere, as a consequence of the switching of the climatological eastward wind to the westward direction due to SSW. Figure 9c also indicates, in orange shading, areas where the meridional gradient of the quasi-geostrophic potential vorticity, $\overline{q}_y$, is negative. The collocation between the critical surfaces and the regions of negative $\overline{q}_y$, along with the emergence of the wave number 1 EP flux vectors from that region strongly suggest the occurrence of barotropic or baroclinic jet instability [e.g., *Charney and Stern*, 1962]. Thus, Figure 9c points to the generation of unstable westward propagating waves (~5–12 days period); the EP flux

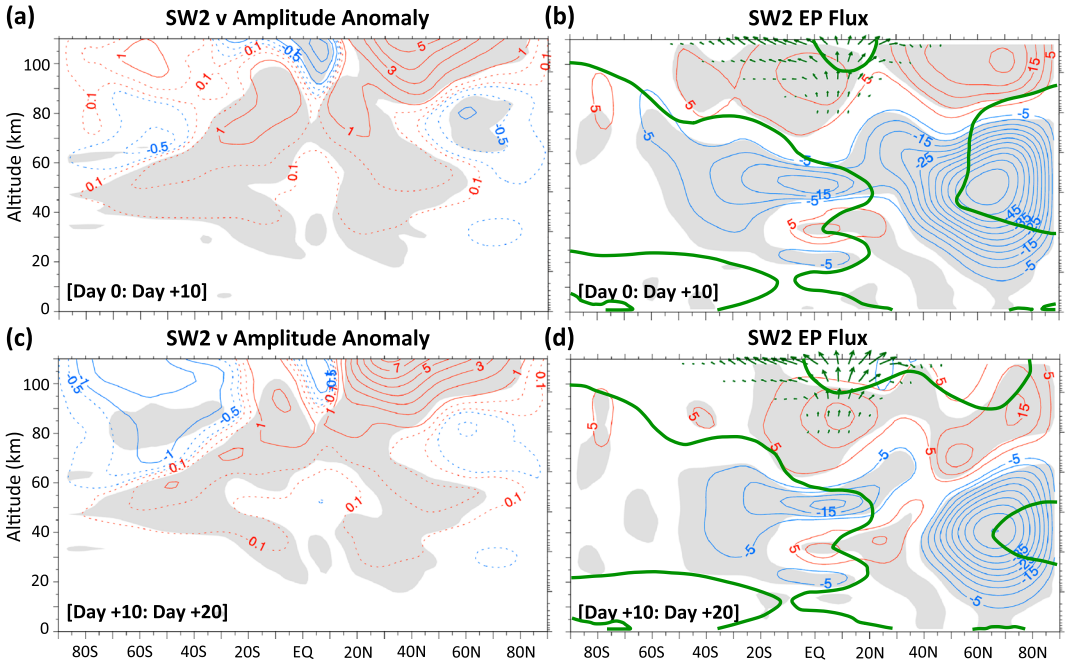

Figure 11. Meridional cross sections of ES-SSW composite of (a, c) meridional wind amplitude anomaly and (b, d) EP flux associated with the migrating semidiurnal tide (SW2). Figures 11a and 11b show the time average over Day 0 to Day 10 (Stage I). Figures 11c and 11d show the time average over Day 10 to Day 20 (Stage II). In Figures 11a and 11c, red contours indicate positive amplitude anomalies and blue contours negative amplitude anomalies, all in m s^{-1}. Red dashed contours show the 0.5 and 0.1 m s^{-1} contours. Blue dashed contours show the −0.5 and −0.1 m s^{-1} contours. In Figures 11b and 11d, the corresponding zonal-mean zonal wind anomalies (red/blue contours) are also shown every 5 m s^{-1}, and the zero wind contour is shown in bold green line for reference (as in Figure 5). Grey shadings indicate regions where the statistical significance level exceeds 95%. Note all EP flux divergence values of SW2 are much less than 5 m s^{-1} d^{-1} and therefore much smaller than the wave drag resulting from PWs and GWs (shown in previous figures).

divergence associated with these waves is the source of the westward drag in the winter polar MLT, consistent with the findings of *Chandran et al.* [2013b]. *Sassi et al.* [2013] and *Sassi and Liu* [2014] likewise report a similar wave number 1 PW signature in the MLT after SSW onset and discuss its possibility as a Rossby normal mode, amplified by jet instability.

6. Tidal Response

Figures 7b and 7d show the enhancement of ozone in the tropical band between 20°S and 20°N in the altitude range of 30 km to 50 km. Figure 5 suggests that this positive ozone anomaly in the tropical stratosphere results from the induced upwelling and cooling forced by westward PW drag. Since the interaction of solar radiation with stratospheric ozone (through UV absorption) is one of the sources of excitation of the migrating semidiurnal tide [*Chapman and Lindzen*, 1970; *Hagan et al.*, 1999; *Sridharan et al.*, 2012], we expect to see a response in amplitude of the migrating semidiurnal tide (SW2). In the case study of the 2009 SSW, *Goncharenko et al.* [2012] observe that the circulation change (induced by PW forcing) can increase the tropical ozone density and, therefore, the excitation of the SW2 tide that perturbs the ionospheric total electron content.

Figure 11 shows the SW2 meridional wind amplitude anomaly and EP flux for Stage I (Figures 11a and 11b) and Stage II (Figures 11c and 11d). The composite structures of the amplitude anomaly and EP flux are similar in both stages. Generally, a large (and significant) positive anomaly in the amplitude exists throughout most of the winter hemisphere above 80 km and the EP flux vectors point upward and poleward over the equator with increasing altitude. We note relatively small wave forcing by SW2, so the role of this tide in driving the circulation (not shown) is negligible compared to that of the GW and PW discussed in section 5. The most notable change in Stage II is the enhancement in the SW2 amplitude anomaly in the winter hemisphere. Along with this change, we see greater wave activity directed toward the winter extratropics (note that the vectors in both stages are scaled with the same reference length).

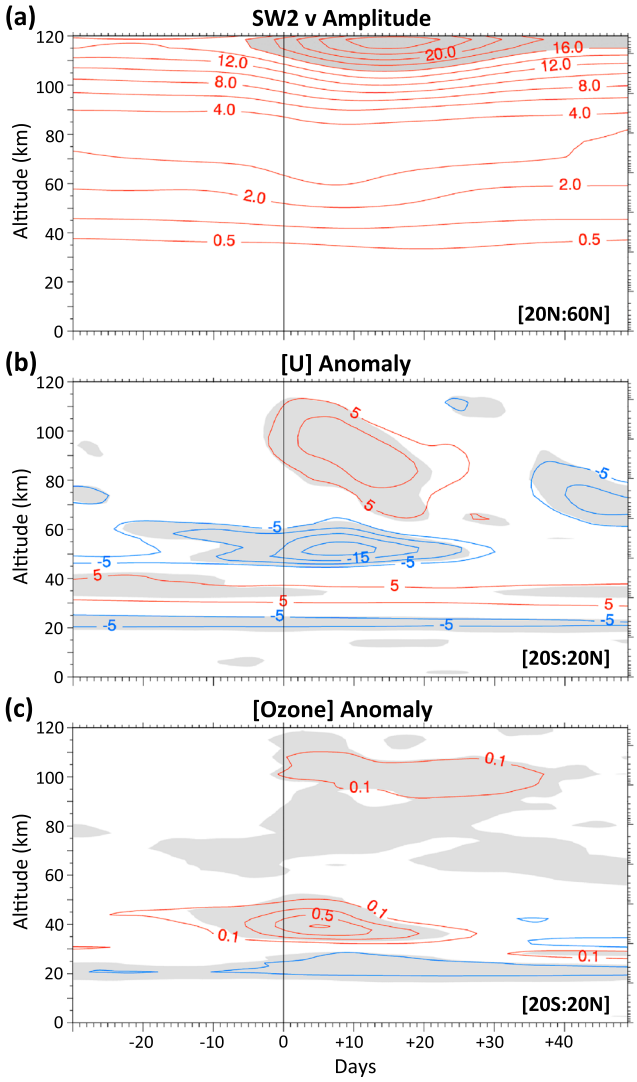

Figure 12. Altitude-time section of ES-SSW composite of (a) meridional wind amplitude of migrating semidiurnal tide (in m s^{-1}), (b) zonal-mean zonal wind anomaly (in m s^{-1}), and (c) zonal-mean ozone anomaly (in parts per million by volume). On the abscissa, time is relative to the ES-SSW onset (i.e., Day 0). In Figure 12a, amplitude values greater than 16 m s^{-1} are shaded to highlight amplification after Day 0. In Figures 12b and 12c, grey shadings are regions where the statistical significance level is above 95%. The latitudinal average band for these quantities is indicated in the lower right corner of each panel.

The evolution of the SW2 amplitude in the winter hemisphere can be seen in Figure 12, where we have extended the altitude range of the plot to 120 km, which starts to encroach on the sponge layer of the model. Nevertheless, we clearly see the growth in SW2 amplitude after Day 0 as highlighted by the grey shading (Figure 12a). The amplitude actually peaks in Stage II. This behavior is consistent with the amplitude anomalies and EP flux shown in Figure 11.

Consistent with the findings of *Sridharan et al.* [2012] and *Goncharenko et al.* [2012], the connection between SW2 amplitude with the tropical ozone is suggested in Figure 12c. Around 40 km, the positive ozone anomaly maximizes around Day 5, related to the anomalous upwelling and cooling in the tropics. However, we note that significant zonal-mean zonal wind anomalies are also present in the equatorial region as shown for both stages in Figures 11b and 11d. The time evolution of the negative wind anomalies over the equatorial zone (Figure 12b) tends to parallel the ozone evolution (Figure 12c) but over a slightly higher altitude range. Given the climatological equatorial zonal-mean westward zonal wind between 40 km and 60 km (as reflected, for example, in Figures 5a and 6a), the negative wind anomalies can enhance the background westward wind and, thereby, the meridional shear of the zonal wind along the winter subtropics. As suggested by

McLandress [2002] for the diurnal tide, the enhancement of meridional wind shear can increase tidal amplitude by broadening the tropical waveguide. Potentially, this shear enhancement may also play a similar role for the SW2 amplitude growth noted here, as suggested by *Sassi et al*. [2013] following the 2009 SSW event (see their Figure 8). Therefore, as concluded by *Jin et al*. [2012], both changes in tropical ozone and background wind may be impacting tidal amplitude and variability.

7. Discussion

The occurrence of zonal-mean zonal wind reversal during a major SSW can be associated with the displacement of the winter polar vortex or the split of the vortex into two smaller vortices. The former type of evolution points to the amplification of PW wave number 1 in initiating SSW while the later is associated with wave number 2. As observed by *Charlton and Polvani* [2007], nearly half of the major SSWs are related to vortex splitting at the 10 hPa level. Using output of free-running WACCM simulations (conducted for the second Chemistry-Climate Model Validation Activity of the Stratospheric Process and their Role in Climate, CCMVal2), *Chandran et al*. [2013a] found that not all SSWs are associated with the elevated stratopause phenomenon. Furthermore, while vortex displacement SSW events occur more frequently than vortex splitting events, nearly 70% of ES-SSW events are associated with vortex splitting. Similarly, based on another free-running model (with perpetual January condition), *Zülicke and Becker* [2013] report a similar tendency toward vortex splitting ES-SSW but note that forcing of the PW wave number 2 is too strong in their model.

In SD-WACCM, the atmosphere below roughly 50 km is constrained by the MERRA reanalyses. Given that we only identified 13 ES-SSW events (due the duration of the available simulation period), we purposely did not divide the ES-SSW events further into those associated with wave numbers 1 and 2. This is to maintain statistical robustness with more composite samples and to keep our analysis simple. However, inspection of the geopotential maps around 10 hPa (not shown) reveals that only two of the selected ES-SSW events (with onset dates of 21 January 2009 and 24 January 1995, as indicated in Figure 1) are characterized by a vortex split (wave number 2). Furthermore, our analyses do not consider the different phases of the QBO. The altered wind direction in the tropical lower stratosphere may potentially impact PW and their interaction with the winter eastward jet, as well as tidal amplitudes [*McLandress*, 2002; *Sassi et al*., 2013].

Based on specialized WACCM runs for a perpetually repeating year, *Holt et al*. [2013] suggest some seasonal dependence of w^* during ES-SSW. They find w^* to be stronger earlier in the winter season. As seen in Figure 1, the onset date mostly occurs in December and January. To investigate seasonal dependence, we further divide our composite into two groups: those with onset in December (five events) and those in January (seven events). Given the low number of events in these groups and different model setup done here, the resulting composites (not shown) only suggest slightly stronger w^* in December after the stratopause reformation in SD-WACCM, as noted by *Holt et al*. [2013].

The predominance of wave number 1 SSW (associated with vortex displacement) may impact the composite result in the MLT. As shown in Figure 2b, the zonal-mean zonal wind (averaged between 60°N and 80°N) between 75 and 80 km switches to westward about 5 days before the ES-SSW onset. For the 2009 ES-SSW, characterized by a vortex split, *Coy et al*. [2011] suggest that this behavior may be considered a mesospheric precursor of this ES-SSW event and highlight the importance of wave number 2 activity and its forcing prior to SSW that leads to the early wind reversal. Furthermore, *Iida et al*. [2014] suggest that instabilities in the middle and upper mesosphere may be the source of this large-scale wave disturbance before the 2009 ES-SSW onset. Whether the split event of 2009 is unique in that respect deserves further investigations. Dominated by wave number 1 SSW, our composite lacks contributions from the wave number 2 activity. Subsequently, a mesospheric precursor is not evident in the composite as suggested by the $[u]$ anomalies (in Figure 3a), which appear nearly simultaneous at all levels. Regardless, *McLandress et al*. [2013] note that the zonal-mean mesospheric response to a major SSW tends to be very similar even though the synoptic structure of wave events may be different.

Our composite results show the presence of westward propagating, wave number 1 PW with periods between 5 and 12 days in the winter MLT during the 30 day period after SSW onset. The associated EP flux imposes a strong westward drag above the mesospheric eastward jet. *Chandran et al*. [2013b] found a very similar PW disturbance in the MLT after the 2011–2012 ES-SSW event onset in the SD-WACCM

simulation and temperature observations by the Sounding of the Atmosphere using the Broadband Emission Radiometry (SABER) instrument onboard NASA's Thermosphere-Ionosphere-Mesosphere Energetics and Dynamics (TIMED) satellite. The westward drag imposed by this PW in that particular winter appears at a similar location and is of similar magnitude as the composite result documented here. The presence of MLT PW amplitudes is also observed in the composite SuperDARN radar observations of *Stray et al*. [2015]. In their study of a model-generated ES-SSW event, *Tomikawa et al*. [2012] likewise note the occurrence of westward propagating wave number 1 PW following the stratospheric wind reversal. However, the PW activity found in that study is confined between 50 and 60 km and may be due to the upper boundary of that model being around 80 km, which kept the reformed stratopause at a much lower altitude.

In agreement with the case studies of *Limpasuvan et al*. [2012] and *Chandran et al*. [2013b], the current composite results clearly point to westward drag by PW as being very important in the vortex recovery from the ES-SSW. For example, in Stage I, we see the dominance of the westward PW drag over the eastward drag in the MLT in driving the initial polar descent (Figure 5). In Stage II, the lingering westward PW drag acts synergistically with the return of the westward GW drag to drive yet stronger winter polar descent and the stratopause reformation at the elevated level (Figure 6). As noted by *Chandran et al*. [2013a] using WACCM unconstrained by analyses, GW driving is always present during ES formation while PW forcing may not. Here based on our selection criteria which favor wave number 1 SSW, nearly all of the selected ES-SSW events in WACCM-SD exhibit PW dominance in Stage I (prior to ES formation) and its contribution during ES formation, as reflected in the composite results.

A thorough instability analysis (e.g., using the linearized quasi-geostrophic potential vorticity equation in a realistic background flow) is not carried out here. However, our composite results suggest that the westward propagating, wave number 1 PW in the winter MLT is a manifestation of the westward jet instability. High-latitude jet instability leading to the generation of a similar type of PW is noted by *Liu et al*. [2004] following SSW in the winter MLT. *Chandran et al*. [2013b] draw a similar conclusion about the presence of PW disturbance in the MLT after the 2011–2012 ES-SSW event in SD-WACCM. Likewise, the instability analysis of *Tomikawa et al*. [2012] suggests the likelihood of barotropic/baroclinic instability growth of PW from the reversed potential vorticity gradient that accompanies the formation of the anomalous westward jet. These authors show that the EP flux divergence (and the eastward drag) of the PW activity, emerging from wave source in the stratospheric westward jet, contributes to the SSW recovery by counteracting the SSW wind reversal. In our study, we see the predominance of EP flux convergence (and the westward drag) as the unstable PW deposit their momentum in the MLT away from the unstable source region. Given the highly variable nature of unstable wave generation during the various ES-SSW events, the compositing technique may diminish the eastward drag values in the source region noted in *Tomikawa et al*. [2012].

Based on the Advanced-Level Physics High-Altitude (ALPHA) prototype of the Navy Operational Global Atmospheric Prediction System (NOGAPS), *Siskind et al*. [2010] report that the resolved GW forcing (based on the vertical flux of the zonal momentum) above 80 km contributes significantly to the total momentum budget during the 2009 ES-SSW event. While the SD-WACCM is of similar horizontal spatial resolution to a NOGAPS-ALPHA run, we see negligible contribution from the resolved GW forcing compared to PW or to the parameterized GW drag in our SD-WACCM composite (not shown). The model dependency of the role of the resolved GW forcing during ES-SSW warrants further investigations.

In studying the tidal response to ES-SSW, we examined various tidal components (migrating and nonmigrating) and found that only the migrating semidiurnal tide (SW2) exhibits a notable change with SSW onset. As tidal amplitudes tend to become large above 100 km, this limited response in the tidal components may be due to the presence of SD-WACCM's upper boundary. Above 115 km, various wave components may be damped due to the model's sponge layer. In this preliminary examination, we have not looked at the phase variation of SW2. Regardless, amplification of SW2 in connection with the enhanced tropical ozone concentration and tropical wind changes is consistent with the studies of *Sridharan et al*. [2012], *Goncharenko et al*. [2012], *Jin et al*. [2012], and *Sassi et al*. [2013]. In studying the atmospheric tidal and ionospheric response to the 2008–2009 ES-SSW event using a coupled whole atmosphere/ionosphere model, *Wang et al*. [2014] also point to an increase in SW2 amplitude following the SSW onset globally, along with the phase shift to an earlier local time. To this end, our composite results illustrate the potential

for a robust response of tidal perturbations that can affect the ionosphere. However, we caution that the described tidal response to ES-SSW may be affected by the dominance of wave number 1 SSW events in our composite, as noted above.

Meridional cross-section composites illustrate the significant extension of ES-SSW effects well into the summer hemisphere. This extension is due in large part to the mean meridional circulation that induces anomalous changes in temperature (and ozone) as seen in Figure 7 and zonal-mean wind in Figure 11. The large PW forcing (and PW enhancement) associated with SSW contributes substantially to driving the circulation and the resulting anomalies. We note that the temperature structure (Figure 7c) is similar to the thermal pattern discussed in the interhemispheric coupling (IHC) hypothesis discussed in *Karlsson et al*. [2009]. In this hypothesis, anomalous PW drag in the winter hemisphere (not exclusively associated with major SSW) can lead (by ~5–30 days) to the warming of the summer mesopause region and, subsequently, variations in noctilucent clouds [*Karlsson et al*., 2007]. Using free-running WACCM 3.5 simulations and SABER observations, *Tan et al*. [2012] produced global teleconnection (correlation) patterns with strong correspondence between temperature anomalies and the mean meridional circulation anomalies through adiabatic heating/cooling for all Northern Hemispheric winters, not just those associated with major or minor SSW events. They note that the IHC impact in the summer hemisphere may extend well into the thermosphere (~115 km). In our composite, the summer polar warming after SSW onset around 100 km (while present) is not statistically significant. This may be attributable to strong variability in the summer hemisphere MLT region and may impact the IHC mechanism where the perturbations are needed to propagate through the mesosphere and lower thermosphere from the equator to the summer pole—a mechanism that remains unclear, as noted by *Tan et al*. [2012]

The summer mesospheric warmings may not be due solely to IHC. As noted by *Pendlebury* [2012] and *Siskind and McCormack* [2014], a strong westward drag by the QTDW in the summer hemisphere may partially negate the eastward GW drag that is seen climatologically atop the summer westward jet (e.g., Figures 5b and 6b). A diminished GW drag would reduce the summer polar upwelling and result in anomalous warming near the summer mesopause. The presence of QTDW (which becomes strongly amplified between December and March near the upper portion of the summer westward jet) may contribute to the strong variability in the summer hemisphere that complicates the IHC mechanism. *Limpasuvan and Wu* [2009] observe that the QTDW may be enhanced during a major SSW.

8. Conclusions

In the present paper, we provide a robust picture of the dynamics of the MLT in response to major SSW events with elevated stratopause (ES). We composite ES-SSW events generated by WACCM, a global climate-chemistry model that extends from the ground up to about 145 km. The model is constrained toward MERRA reanalyses below 50 km. Realistic SSW conditions above this region are produced by the model. We focus on the role of planetary and gravity waves. From our composite analysis, we arrive at three key points regarding the MLT responses to SSW with ES.

The presence of westward propagating PW is a crucial part of the response of the MLT to the ES-SSW, promoting winter polar descent and the recovery of the stratopause. In the polar winter region, the anomalous westward PW drag in the MLT peaks after SSW onset and persists for about 25 days. This drag is associated primarily with the EP flux convergence of westward propagating, wave number 1 PW activity (with a period between 5 and 12 days) that had propagated upward from an unstable region within the anomalous westward jet below 80 km. This westward PW drag dominates the anomalous eastward GW drag, which was permitted in the MLT by the same underlying westward jet due to major warming. The resulting net westward drag drives a mean circulation with, initially, polar downwelling in the lower thermosphere. As polar warming subsides, the westward PW drag persists and synergistically combines with the return of the westward GW drag (and the underlying eastward jet) to drive a much stronger mean circulation. The resulting strong polar downwelling adiabatically warms the winter pole and promotes the reformation of the stratopause at an elevated altitude.

During ES-SSW, atmospheric tides exert negligible momentum forcing compared to PW and GW within the model domain, but the amplitude of the migrating semidiurnal component undergoes notable amplification. The migrating semidiurnal tide is amplified nearly globally in the 20–30 days after SSW onset. This may be

due to the enhanced stratospheric ozone in the tropics (and associated solar heating) due the equatorial upwelling and cooling associated with the SSW. The associated changes in meridional shear of the equatorial zonal-mean zonal wind may also contribute to further tidal enhancement. The relative roles of ozone anomalies and wind shear on the tidal response warrant further investigations. The amplification of the migrating semidiurnal tidal amplitude is most pronounced in the winter hemisphere above 90 km.

The impact of ES-SSW extends well across the equator, strongly altering the zonal-mean tropical zonal wind, temperature, and ozone distribution. However, the response of the MLT summer region to ES-SSW is not obvious. The anomalous temperature patterns in the mean meridional cross-section 10–20 days after SSW onset resemble those ascribed to the interhemispheric coupling mechanism (IHC) by *Karlsson et al*. [2009]. However, the polar warming in the summer MLT is not significant in the composite results.

Acknowledgments

V.L. is supported in part by the Large-Scale Dynamics Program at the National Science Foundation (NSF) under award AGS-1116123 and the Kerns Palmetto Professorship supported by the Coastal Carolina University's Provost office. Y.O.R. was supported by the Norwegian grant. Y.O.R. is supported at the Birkeland Centre for Space Science by the Research Council of Norway/CoE under contract 223252/F50. The National Center for Atmospheric Research (NCAR) is sponsored by NSF. WACCM is a component of the Community Earth System Model (CESM), which is supported by NSF and the Office of Science of the U.S. Department of Energy. CESM and the files needed to run it are available from NCAR; see https://www2.cesm.ucar.edu/models/current. The authors are grateful to Doug Kinnison at NCAR for his help in setting up the model simulations and the anonymous reviewers for their suggestions and input. Data for this study can be accessed by contacting the corresponding author.

References

Andrews, D. G., J. R. Holton, and C. B. Leovy (1987), *Middle Atmosphere Dynamics*, 489 pp., Academic Press, New York.

Baldwin, M. P., and T. J. Dunkerton (2001), Stratospheric harbingers of anomalous weather regimes, *Science*, *294*, 581–584.

Butler, A. H., D. J. Seidel, S. C. Hardiman, N. Butchart, T. Birner, and A. Match (2015), Defining sudden stratospheric warmings, *Bull. Am. Meteorol. Soc.*, *96*, 1913–1928, doi:10.1175/BAMS-D-13-00173.1.

Chandran, A., R. L. Collins, R. R. Garcia, D. R. Marsh, V. L. Harvey, J. Yue, and L. de la Torre (2013a), A climatology of elevated stratopause events in the whole atmosphere community climate model, *J. Geophys. Res. Atmos.*, *118*, 1234–1246, doi:10.1002/jgrd.50123.

Chandran, A., R. R. Garcia, R. L. Collins, and L. C. Chang (2013b), Secondary planetary waves in the middle and upper atmosphere following the stratospheric sudden warming event of January 2012, *Geophys. Res. Lett.*, *40*, 1861–1867, doi:10.1002/grl.50373.

Chandran, A., R. L. Collins, and V. L. Harvey (2014), Stratosphere-mesosphere coupling during stratospheric sudden warming events, *Adv. Space Res.*, *53*(9), 1265–1289, doi:10.1016/j.asr.2014.02.005.

Chapman, S., and R. L. Lindzen (1970), *Atmospheric Tides*, 200 pp., Gordon and Breach, New York.

Charlton, A. J., and L. M. Polvani (2007), A new look at stratospheric sudden warmings. Part I: Climatology and modeling benchmarks, *J. Clim.*, *20*, 449–469, doi:10.1175/JCLI3996.1.

Charney, J. G., and M. E. Stern (1962), On the stability of internal baroclinic jets in a rotating atmosphere, *J. Atmos. Sci.*, *19*, 159–172.

Coy, L., S. D. Eckermann, K. W. Hoppel, and F. Sassi (2011), Mesospheric precursors to the major stratospheric sudden warming of 2009: Validation and dynamical attribution using a ground-to-edge-of-space data assimilation system, *J. Adv. Model. Earth Syst.*, *3*, M10002, doi:10.1029/2011MS000067.

De Wit, R. J., R. E. Hibbins, P. J. Espy, Y. J. Orsolini, V. Limpasuvan, and D. Kinnison (2014), Observations of gravity wave forcing of the mesopause region during the January 2013 major sudden stratospheric warming, *Geophys. Res. Lett.*, *41*, 4745–4752, doi:10.1002/2014GL060501.

Fritz, S., and S. D. Soules (1970), Large-scale temperature changes in the stratosphere observed from Nimbus III, *J. Atmos. Sci.*, *27*, 1091–1097.

Garcia, R. R., and B. A. Boville (1994), "Downward control" of the mean meridional circulation and temperature distribution of the polar winter stratosphere, *J. Atmos. Sci.*, *51*, 2238–2245.

Goncharenko, L., A. Coster, R. Plumb, and D. Domeisen (2012), The potential role of stratospheric ozone in the stratosphere-ionosphere coupling during stratospheric warmings, *Geophys. Res. Lett.*, *39*, L08101, doi:10.1029/2012GL051261.

Hagan, M. E., M. D. Burrage, J. M. Forbes, J. Hackney, W. J. Randel, and X. Zhang (1999), GSWM-98: Results for migrating solar tides, *J. Geophys. Res.*, *104*, 6813–6827, doi:10.1029/1998JA900125.

Hitchman, M. H., J. C. Gille, C. D. Rodgers, and G. Brasseur (1989), The separated polar winter stratopause: A gravity wave driven climatological feature, *J. Atmos. Sci.*, *46*, 4310–422.

Hoffmann, C. G., D. E. Kinnison, R. R. Garcia, M. Palm, J. Notholt, U. Raffalski, and G. Hochschild (2012), CO at 40–80 km above Kiruna observed by the ground-based microwave radiometer KIMRA and simulated by the Whole Atmosphere Community Climate Model, *Atmos. Chem. Phys.*, *12*, 3261–3271.

Holt, L. A., C. E. Randall, E. D. Peck, D. R. Marsh, A. K. Smith, and V. L. Harvey (2013), The influence of major sudden stratospheric warming and elevated stratopause events on the effects of energetic particle precipitation in WACCM, *J. Geophys. Res. Atmos.*, *118*, 11,636–11,646, doi:10.1002/2013JD020294.

Holton, J. R. (1983), The influence of gravity wave breaking on the general circulation of the middle atmosphere, *J. Atmos. Sci.*, *40*, 2497–2507.

Iida, C., T. Hirooka, and N. Eguchi (2014), Circulation changes in the stratosphere and mesosphere during the stratospheric sudden warming event in January 2009, *J. Geophys. Res. Atmos.*, *119*, 7104–7115, doi:10.1002/2013JD021252.

Jin, H., Y. Miyoshi, D. Pancheva, P. Mukhtarov, H. Fujiwara, and H. Shinagawa (2012), Response of migrating tides to the stratospheric sudden warming in 2009 and their effects on the ionosphere studied by a whole atmosphere-ionosphere model GAIA with COSMIC and TIMED/SABER observations, *J. Geophys. Res.*, *117*, A10323, doi:10.1029/2012JA017650.

Karlsson, B., H. Kornich, and J. Gumbel (2007), Evidence for interhemispheric stratosphere-mesosphere coupling derived from noctilucent cloud properties, *Geophys. Res. Lett.*, *43*, L16806, doi:10.1029/2007GL030282.

Karlsson, B., C. McLandress, and T. G. Shepherd (2009), Inter-hemispheric mesospheric coupling in a comprehensive middle atmosphere model, *J. Atmos. Sol. Terr. Phys.*, *71*, 518–530, doi:10.1016/j.jastp.2008.08.006.

Kushner, P. J. (2011), Annular modes of the troposphere and stratosphere, in *The Stratosphere: Dynamics, Transport, and Chemistry*, *Geophys. Monogr. Ser.*, vol. 190, edited by L. M. Polvani, A. H. Sobel, and D. W. Waugh, pp. 59–91, AGU, Washington, D. C.

Kvissel, O.-K., Y. J. Orsolini, F. Stordal, V. Limpasuvan, J. H. Richter, and D. R. Marsh (2012), Mesospheric intrusion and anomalous chemistry during and after a major stratospheric sudden warming, *J. Atmos. Sol. Terr. Phys.*, *78–79*, 116–124, doi:10.1016/j.jastp.2011.08.015.

Lee, J. N., D. L. W. G. L. Manney, M. J. Schwartz, A. Lambert, N. J. Livesey, K. R. Minschwaner, H. C. Pumphrey, and W. G. Read (2010), Aura microwave limb sounder observations of the polar middle atmosphere: Dynamics and transport of CO and H_2O, *J. Geophys. Res.*, *116*, D05110, doi:10.1029/2010JD014608.

Limpasuvan, V., and D. L. Hartmann (2000), Wave-maintained annular modes of climate variability, *J. Clim.*, *13*, 4414–4429.

Limpasuvan, V., and D. L. Wu (2009), Anomalous Two-day wave behavior during the 2006 Austral summer, *Geophys. Res. Lett.*, *36*, L04807, doi:10.1029/2008GL036387.
Limpasuvan, V., D. W. J. Thompson, and D. L. Hartmann (2004), The life cycle of Northern Hemisphere sudden stratospheric warmings, *J. Clim.*, *17*, 2584–2596.
Limpasuvan, V., D. L. Wu, M. J. Schwartz, J. W. Waters, Q. Wu, and T. L. Killeen (2005), The two-day wave in EOS MLS temperature and wind measurements during 2004–2005 winter, *Geophys. Res. Lett.*, *32*, L17809, doi:10.1029/2005GL023396.
Limpasuvan, V., J. H. Richter, Y. J. Orsolini, F. Stordal, and O.-K. Kvissel (2012), The roles of planetary and gravity waves during a major stratospheric sudden warming as characterized by WACCM, *J. Atmos. Sol. Terr. Phys.*, *78–79*, 84–98.
Liu, H.-L., and R. G. Roble (2002), A study of a self-generated stratospheric sudden warming and its mesospheric-lower thermospheric impacts using the coupled TIME-GCM/CCM3, *J. Geophys. Res.*, *107*(D23), 4695, doi:10.1029/2001JD001533.
Liu, H.-L., E. R. Talaat, R. G. Roble, R. S. Lieberman, D. M. Riggin, and J.-H. Yee (2004), The 6.5-day wave and its seasonal variability in the middle and upper atmosphere, *J. Geophys. Res.*, *109*, D21112, doi:10.1029/2004JD004795.
Manney, G. L., et al. (2008), The evolution of the stratopause during the 2006 major warming: Satellite data and assimilated meteorological analyses, *J. Geophys. Res.*, *113*, D11115, doi:10.1029/2007JD009097.
Manney, G. L., M. J. Schwartz, K. Krüger, M. L. Santee, S. Pawson, J. N. Lee, W. H. Daffer, R. A. Fuller, and N. J. Livesey (2009), Aura Microwave Limb Sounder observations of dynamics and transport during the record-breaking 2009 Arctic stratospheric major warming, *Geophys. Res. Lett.*, *36*, L12815, doi:10.1029/2009GL038586.
Marsh, D. R. (2011), Chemical–dynamical coupling in the mesosphere and lower thermosphere, in *Aeronomy of the Earth's Atmosphere and Ionosphere*, *IAGA Spec. Sopron Book Ser.*, vol. 2, pp. 3–17, Springer, Netherlands.
Marsh, D. R., M. E. Mills, D. E. Kinnison, J.-F. Lamarque, N. Calvo, and L. M. Polvani (2013), Climate change from 1850 to 2005 simulated in CESM1 (WACCM), *J. Clim.*, *26*, 7372–7391, doi:10.1175/JCLI-D-12-0558.1.
Matsuno, T. (1971), A dynamical model of the stratospheric sudden warming, *J. Atmos. Sci.*, *28*, 1479–1494.
McLandress, C. (2002), The seasonal variation of the propagating diurnal tide in the mesosphere and lower thermosphere. Part II: The role of tidal heating and zonal mean winds, *J. Atmos. Sci.*, *59*, 907–922.
McLandress, C., J. F. Scinocca, T. G. Shepherd, M. C. Reader, and G. L. Manney (2013), Dynamical control of the mesosphere by orographic and nonorographic gravity wave drag during the extended northern winters of 2006 and 2009, *J. Atmos. Sci.*, *70*(7), 2152–2169, doi:10.1175/JAS-D-12-0297.1.
Orsolini, Y. J., J. Urban, D. P. Murtagh, S. Lossow, and V. Limpasuvan (2010), Descent from the polar mesosphere and anomalously high stratopause observed in 8 years of water vapor and temperature satellite observations by the Odin Sub-Millimeter Radiometer, *J. Geophys. Res.*, *115*, D12305, doi:10.1029/2009JD013501.
Pendlebury, D. (2012), A simulation of the quasi-two-day wave and its effect on variability of summertime mesopause temperatures, *J. Atmos. Sol. Terr. Phys.*, *80*, 138–151.
Randall, C. E., et al. (2005), Stratospheric effects of energetic particle precipitation in 2003–2004, *Geophys. Res. Lett.*, *32*, L05802, doi:10.1029/2004GL022003.
Randall, C. E., V. L. Harvey, D. E. Siskind, J. France, P. F. Bernath, C. D. Boone, and K. A. Walker (2009), NO_x descent in the Arctic middle atmosphere in early 2009, *Geophys. Res. Lett.*, *36*, L18811, doi:10.1029/2009GL039706.
Randall, C. E., V. L. Harvey, L. A. Holt, D. R. Marsh, D. Kinnison, B. Funke, and P. F. Bernath (2015), Simulation of energetic particle precipitation effects during the 2003–2004 Arctic winter, *J. Geophys. Res. Space Physics*, *120*, 5035–5048, doi:10.1002/2015JA021196.
Randel, W. J. (1993), Global variations of zonal mean zonal ozone during stratospheric warming events, *J. Atmos. Sci.*, *50*, 3308–3321.
Richter, J. H., F. Sassi, and R. R. Garcia (2010), Toward a physically based gravity wave source parameterization in a general circulation model, *J. Atmos. Sci.*, *67*, 136–156, doi:10.1175/2009JAS3112.1.
Rienecker, M. M., et al. (2011), MERRA: NASA's modern-era retrospective analysis for research and applications, *J. Clim.*, *24*, 3624–3648, doi:10.1175/JCLI-D-11-00015.1.
Sassi, F., and H.-L. Liu (2014), Westward traveling planetary wave events in the lower thermosphere during solar minimum conditions simulated by SD-WACCM-X, *J. Atmos. Sol. Terr. Phys.*, *119*, 11–26.
Sassi, F., H.-L. Liu, J. Ma, and R. R. Garcia (2013), The lower thermosphere during the Northern Hemisphere winter of 2009: A modeling study using high-altitude data assimilation products in WACCM-X, *J. Geophys. Res. Atmos.*, *118*, 8954–8968, doi:10.1002/jgrd.50632.
Siskind, D. E., and J. P. McCormack (2014), Summer mesospheric warmings and the quasi 2 day wave, *Geophys. Res. Lett.*, *41*, 717–722, doi:10.1002/2013GL058875.
Siskind, D. E., L. Coy, and P. Espy (2005), Observations of stratospheric warmings and mesospheric coolings by the TIMED SABER instrument, *Geophys. Res. Lett.*, *32*, L09804, doi:10.1029/2005GL022399.
Siskind, D. E., S. D. Eckermann, L. Coy, J. P. McCormack, and C. E. Randall (2007), On recent interannual variability of the Arctic winter mesosphere: Implications for tracer descent, *Geophys. Res. Lett.*, *34*, L09806, doi:10.1029/2007GL029293.
Siskind, D. E., S. D. Eckermann, J. P. McCormack, L. Coy, K. W. Hoppel, and N. L. Baker (2010), Case studies of the mesospheric response to recent minor, major, and extended stratospheric warmings, *J. Geophys. Res.*, *115*, D00N03, doi:10.1029/2010JD014114.
Siskind, D. E., F. Sassi, C. E. Randall, V. L. Harvey, M. E. Hervig, and S. M. Bailey (2015), Is a high-altitude meteorological analysis necessary to simulate thermosphere-stratosphere coupling?, *Geophys. Res. Lett.*, *42*, 8225–8230, doi:10.1002/2015GL065838.
Smith, A. K. (1996), Longitudinal variations in mesospheric winds: Evidence for gravity wave filtering by planetary waves, *J. Atmos. Sci.*, *53*, 1156–1173.
Smith, A. K. (2003), The origin of stationary planetary waves in the upper mesosphere, *J. Atmos. Sci.*, *60*, 3033–3041.
Smith, A. K., M. Lopez-Puertas, M. Garcia-Comas, and S. Tukiainen (2009), SABER observations of mesospheric ozone during NH late winter 2002–2009, *Geophys. Res. Lett.*, *36*, L23804, doi:10.1029/2009GL040942.
Sridharan, S., S. Sathishkumar, and S. Gurubaran (2012), Variabilities of mesospheric tides during sudden stratospheric warming events of 2006 and 2009 and their relationship with ozone and water vapour, *J. Atmos. Sol. Terr. Phys.*, *78–79*, 108–115, doi:10.1016/j.jastp.2011.03.013.
Stray, N. H., Y. J. Orsolini, P. J. Espy, V. Limpasuvan, and R. E. Hibbins (2015), Observations of planetary waves in the mesosphere-lower thermosphere during stratospheric warming events, *Atmos. Chem. Phys.*, *15*, 4997–5005, doi:10.5194/acp-15-4997-2015.
Tan, B., X. Chu, H.-L. Liu, C. Yamashita, and J. M. Russell III (2012), Zonal-mean global teleconnection from 15 to 110 km derived from SABER and WACCM, *J. Geophys. Res.*, *117*, D10106, doi:10.1029/2011JD016750.
Tomikawa, Y., K. Sato, S. Watanabe, Y. Kawatani, K. Miyazaki, and M. Takahashi (2012), Growth of planetary waves and the formation of an elevated stratopause after a major stratospheric sudden warming in a T213L256 GCM, *J. Geophys. Res.*, *117*, D16101, doi:10.1029/2011JD017243.

Tweedy, O. V., et al. (2013), Nighttime secondary ozone layer during major stratospheric sudden warmings in specified-dynamics WACCM, *J. Geophys. Res. Atmos.*, *118*, 8346–8358, doi:10.1002/jgrd.50651.

Wang, H., R. A. Akmaev, T.-W. Fang, T. J. Fuller-Rowell, F. Wu, N. Maruyama, and M. D. Iredell (2014), First forecast of a sudden stratospheric warming with a coupled whole-atmosphere/ionosphere model IDEA, *J. Geophys. Res. Space Physics*, *119*, 2079–2089, doi:10.1002/2013JA019481.

Wu, D. L., M. J. Schwartz, J. W. Waters, V. Limpasuvan, Q. Wu, and T. L. Killeen (2008), Mesospheric Doppler Wind measurements from Aura Microwave Limb Sounder (MLS), *Adv. Space Res.*, *42*, 1246–1252, doi:10.1016/j.asr.2007.06.014.

Zülicke, C., and E. Becker (2013), The structure of the mesosphere during sudden stratospheric warmings in a global circulation model, *J. Geophys. Res. Atmos.*, *118*, 2255–2271, doi:10.1002/jgrd.50219.